ARTICLE OPEN

Check for updates

Bio-inspired self-healing and anti-corrosion waterborne polyurethane coatings based on highly oriented graphene oxide

Lin Wang[1,2,3], Xuebin Wang[1,3], Tong Liu[1], Fuyao Sun[1], Suning Li[1], Yuhao Geng[1], BoWen Yao[1]✉, Jianhua Xu[1,2]✉ and JiaJun Fu[1]✉

In the face of ubiquitous corrosion threats, the development of high-performance elastomer protective materials with active self-healing functions is extremely challenging and significant. We propose an approach by combining WPU elastomer with GO to create the multifunctional pearl layer structured polymers with interface hydrogen bonds. By crosslinking the polycaprolactone diol (PCL) chain with a hydrogen bond array, the elastomer with high mechanical strength, extensibility, elasticity, excellent damage resistance, and healing properties was successfully synthesized. The elastomer exhibits remarkable mechanical properties, including a tensile strength of 39.89 MPa, toughness value of 300.3 MJ m^{-3}, and fracture energy of 146.57 kJ m^{-2}. The enhanced damage resistance of the elastomer can be attributed to the decomposable hydrogen bond array as well as the strain-induced crystallization of PCL fragments, which effectively dissipate energy. Importantly, due to the reversibility of the hydrogen bonding array, the fractured WPU can easily heal and restore its original mechanical properties when subjected to heating at 50 °C. Moreover, the photothermal properties of GO enable the biomimetic polymer coating to achieve damage recovery after being irradiated with NIR for 30 s. The obtained biomimetic coating exhibits a highly oriented lamellar structure, thereby greatly enhancing physical barrier performance and anti-corrosion performance. Electrochemical impedance spectroscopy (EIS) shows that the impedance modulus is one order of magnitude higher than that of the blank coating. Additionally, scanning vibrating electrode (SVET) confirmed that the self-healing performance and protection effect of the biomimetic coating in 3.5 wt% NaCl solution were also reliable. This highly reliable biomimetic coating presents a revolutionary solution for creating multi-functional, high-performance smart material in harsh environments.

npj Materials Degradation (2023)7:96 ; https://doi.org/10.1038/s41529-023-00415-9

INTRODUCTION

Steel, led by carbon steel, has become the most important alloy in various engineering applications owing to its low price and high strength[1]. However, the lattice spacing of iron oxide (rust) is much larger than that of iron. And when corrosion occurs, the rust will naturally separate and form a porous structure[2]. This porous structure makes it easy for water and oxygen to diffuse and peel off, which does not provide protection against further corrosion of the underlying steel plate[3]. The anti-corrosion capability of steel is poor, thus protective measures need to be taken in corrosive environments[4]. Cl^- can penetrate and destroy oxides on metal surfaces and accelerate metal corrosion, making it the most corrosive environment for steel to date. Water and O_2 are essential conditions for the early stages of steel corrosion. Coating technology can hinder the invasion of water and O_2[5]. Currently, ultra-thin, efficient, and durable coatings are the most cost-effective, robust, and long-lasting methods for protecting steel. The ideal coating should meet two basic requirements: isolating the metal from corrosive environments and minimizing corrosion damage in the event of isolation failure[6]. Nowadays, metal coatings, polymer coatings, and organic–inorganic hybrid coatings are three commonly applied coatings, which exhibit different levels of anti-corrosion performance based on the protection mechanism and expected combination of metal and environment. Therefore, exploring anti-corrosion materials and/or coating technologies that meet these two requirements is crucial for the advancement of the modern anti-corrosion industry.

The key feature of coatings is to provide protection and decoration for the substrate. Special coatings necessitate multiple functionalities that adjust to specific environmental demands. However, upon the coating is damaged, it will lose its function. Moreover, after the coating on the substrate is completed, the damage to the coating is related to factors such as transportation and application environment. If these coating damages are not repaired on time, they will lead to damage to the protected substrate and may even lead to safety accidents. However, using traditional passive manual repair technology has many issues such as the inability to detect and repair promptly, time-consuming repair, and high repair costs. Inspired by the inherent ability of biological "passive damage active repair", intelligent self-healing anti-corrosion polymer coatings can heal by themselves within an effective time after coating damage occurs, thereby eliminating safety hazards caused by coating damage and extending service life[7]. Most importantly, they achieve multiple reversible repairs through reversible fracture recombination or dynamic exchange of chemical bonds in their systems[8]. At present, it has been evidenced to be more effective in extending the lifespan, safety, and reliability of engineering coatings compared to traditional polymer coatings with a single anti-permeability performance, especially in high-durability structures[9].

Among many polymers, waterborne polyurethane (WPU) with water as the dispersion medium has attracted considerable attention due to its advantages of pollution-free, safe and reliable, strong adhesion, and good compatibility[8,10]. Since WPU must be a stable dispersion, one way may introduce certain hydrophilic

[1]School of Chemistry and Chemical Engineering, Nanjing University of Science and Technology, 210094 Nanjing, P. R. China. [2]Joint Laboratory of Advanced Biomedical Materials (NFU-UGent), College of Chemical Engineering, Nanjing Forestry University, 210037 Nanjing, P. R. China. [3]These authors contributed equally: Lin Wang, Xuebin Wang.
✉email: bowenyao@njust.edu.cn; xujianhua931118@163.com; fujiajun668@gmail.com

groups (–COOH) during the reaction process. Thereby, the water resistance, solvent resistance, density, and shrinkage of the coating will be correspondingly reduced[11]. Another way is to reduce the crosslinking degree of PU prepolymer to improve the stability of WPU dispersion. Therefore, due to the low crosslinking degree and many hydrophilic polar groups, the corrosion resistance of WPU coatings is not satisfactory[12]. The urgent requirement to develop intelligent anti-corrosion coatings with exceptional barrier performance and outstanding self-healing capabilities through modification represents a significant technical challenge.

Graphene (Gr) and graphite oxide (GO) nanosheets can be used as enhancement projects of functional bionic materials because of their outstanding physical barrier effect, mechanical strength, and chemical stability[13–15]. Prasai et al. confirmed that monolayer Gr grown through chemical vapor deposition (CVD) can effectively protect copper oxidation, and received strong support from various simulations[16]. Interestingly, Schriver's group evidenced that due to the presence of defects, CVD Gr coatings can accelerate local corrosion for long periods[17]. Due to the fact that defects in the coating (local anode) can affect its anti-corrosion performance, it is crucial to prevent the formation of defects in the design and manufacturing of anti-corrosion coatings[18]. To make the coating more sturdy and suitable for practical applications, it is preferable to use nanocomposites instead of single-layer Gr coatings[19]. Uniform dispersion of Gr in nanocomposites is crucial to attain the desired level of anti-corrosion performance. Only when Gr is uniformly dispersed within the nanocomposite can it effectively enhance the anti-corrosion properties[20].

The structure of the layered "brick mud" structural pearl layer possesses functional barriers and ion transport control capacities[21]. In addition, combined with the interaction mechanism between the human immune system and tumor vascular lipids[22]. Cancer cells induce the formation of many new blood vessels to obtain O_2 and nutrients, but these new blood vessels are flawed, with leakage and structural and functional defects. Like the pearl layer of bricks and tiles, normal blood vessels can delay tumor progression. The two ideas provided valuable insights for designing advanced GO-polymer coatings with efficient anti-corrosion performance. At present, various methods have been adopted to synthesize high-orientation barrier structures[20,23]. The complexity and extensive energy consumption of magnetic field induction and electrophoretic deposition, etc., make these processes impractical for large-scale production of coatings, seriously limiting their practical applications[21,24]. Research has shown that spatially stable nanosheets suspended in organic solutions mixed with appropriate prepolymers or polymers can maintain the mesoporous structure of the nanosheets, even after the solvent has been removed. This property allows for the formation of self-assembled smectic layers of nanosheets in the resin through simple spraying and rolling processes[18,25,26]. Therefore, using evaporation-induced self-assembly technology, highly oriented composite materials can be easily and efficiently obtained.

The present study introduced an innovative construction strategy for the development of self-healing highly oriented lamellar biomimetic nanocomposites with functionalized properties. Firstly, a bio-based self-healing elastomer was successfully synthesized. Secondly, GO was incorporated into the polymer matrix. Through a roll coating preparation process and solvent evaporation, GO-nanocomposite lamellar coatings were obtained, featuring enhanced anti-corrosion properties attributed to the hydrogen bonding of the polymer in the system. The non-covalent interactions generated by WPU material within the system not only exhibited remarkable self-healing ability but also contributed significantly to the flexibility of the composite materials. The electrochemical impedance spectroscopy (EIS) and scanning vibrating electrode (SVET) analyses confirmed that the nanocomposite coatings maintained an excellent ability to shield against the penetration of corrosive media in artificial seawater. These findings were further supported by large-scale immersion tests, demonstrating the outstanding anti-corrosion performance of the composite coating. Moreover, the composite coating not only possessed a heating-induced self-healing function but also showed promising results for short-term near-infrared (NIR) light stimulation self-healing. Overall, this designed coating demonstrated excellent dual self-healing, puncture-resistant, stretchable, damage-resistant, and anti-corrosion properties, exhibiting extremely high self-healing efficiency.

RESULTS

Molecular design, physical, mechanical, and self-healing properties of WPU

The procedure for fabricating the supramolecular elastomer was convenient and controllable. WPU elastomers were synthesized through a one-pot polycondensation reaction with a mixture of PCL, HDMI, DMBA, and 4,6-diaminopyrimidine. A polymer film was obtained for subsequent measurements through the solvent-forming process, and no bubbles were observed inside the film. The particle size distribution of the prepared WPU is shown in Fig. 1c, with 26.852% distributed around 10 nm and 27.262% distributed around 11 nm. The optical photograph presented in Fig. 1d depicted the high transparency of WPU.

To verify the existence of multiple hydrogen bonding interactions, in situ temperature-dependent FT-IR spectroscopy was used to further examine these interactions (variable temperature infrared image, Supplementary Fig. 1). The C=O acted as a hydrogen bond receptor. As the temperature increased, the C=O peak shifted from 1724 to 1732 cm^{-1}, and the relative intensity two-dimensional infrared correlation spectroscopy (2D-COS) of WPU in the 1800–1600 cm^{-1} band was calculated (Fig. 1e, f). Two main automatic peaks, namely (1741, 1741 cm^{-1}) and (1705, 1705 cm^{-1}), were observed in the synchronous spectrum. While a main cross peak, namely (1741, 1705 cm^{-1}), was observed in the asynchronous spectrum. According to Nado's law, the order of absorption peaks with increasing temperature was 1705 cm^{-1} → 1741 cm^{-1}. Peaks near 1732 cm^{-1} typically corresponded to ordered C=O groups that participated in hydrogen bonding at low wave numbers, free C=O groups that did not participate in hydrogen bonding at high wave numbers, and disordered C=O groups[10]. The C=O group participated in partial hydrogen bonding at the intermediate wave number. That was to say, the peaks at 1705, 1732, and 1741 cm^{-1} were attributed to ordered C=O, disordered C=O, and free C=O groups, respectively. The response of functional groups with free C=O groups to temperature rise was slower than that of ordered groups. In situ temperature-dependent FTIR spectroscopy and 2D-COS evidenced that as the temperature increased, the peak at 1724 cm^{-1} shifted to 1732 cm^{-1}, indicating that the peak at 1705 cm^{-1} with ordered C=O groups was gradually replaced by the peak at 1741 cm^{-1} with disordered and free C=O groups. The results mentioned above suggested that temperature-dependent variations in the characteristic peak of C=O indicated the presence of hydrogen bond interactions in the material. These hydrogen bonds underwent dissociation and recombination, leading to the observed changes in the peak.

The results presented in Fig. 2a showed that the WPU elastomer followed a typical stress–strain curve, which exhibited classic elastomeric behavior. This meant that this elastomer did not exhibit any yielding phenomena during elongation. The WPU elastomer possessed a tensile strength of ~39.89 MPa and a breaking strain of ~1827.65%, which translated to an exceptionally high toughness of ~300.3 MJ m^{-3}. The introduction of PCL ensured that WPU had better segment motion and mechanical

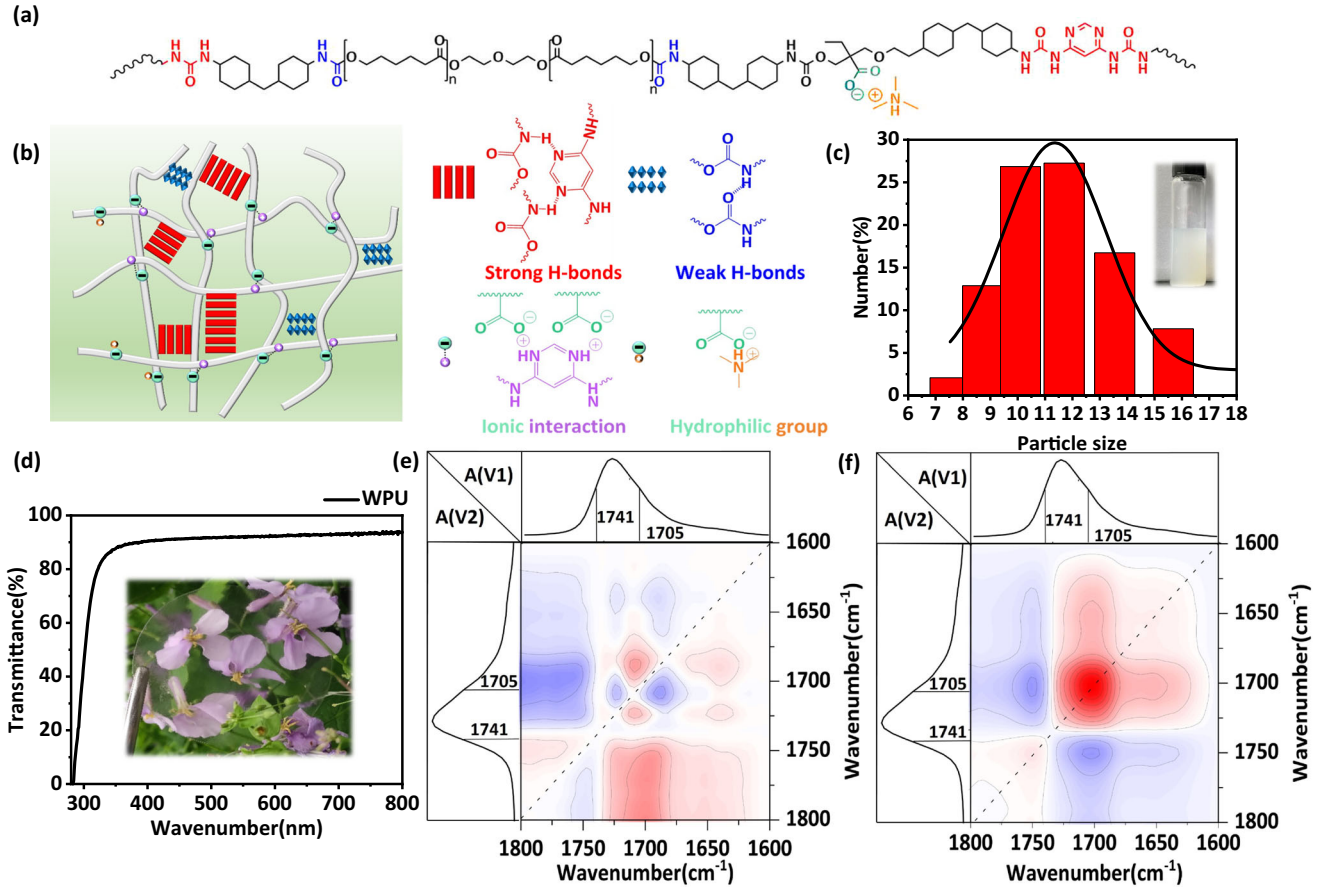

Fig. 1 Molecular design and physical properties of WPU materials. a Molecular design and chemical structure of WPU. **b** Schematic diagram of WPU and its self-assembled network. **c** Particle size distribution of WPU (the optical photograph of the WPU was shown in the illustration). **d** Transmittance of WPU in the visible range (The optical photograph of flowers and plants captured through WPU was shown in the illustration). The **e** synchronous and **f** asynchronous 2D-related FT-IR spectra of WPU were calculated from 30 to 160 °C.

strength. Figure 2b shows that the prepared WPU elastomer could withstand 5.0 kg water. To further evaluate the damage resistance of the WPU elastomer, a needle-impact test was conducted. The ~0.80 mm-thick WPU elastomer sheet could withstand a needle puncture, demonstrating remarkable displacement and enduring force values of ~46.3 mm and ~109.7 N, respectively (Fig. 2c). In addition to damage resistance, the WPU elastomer also exhibited superb damage tolerance. This was demonstrated by subjecting a notched sample of the elastomer (~5 mm in width and ~0.8 mm in length) to stretching. Despite the presence of a notch measuring approximately 1 mm, the elastomer could be stretched up to ~1000% strain without the notch propagating (Fig. 2d and Supplementary Movie 1). This indicated that the WPU elastomer maintained its mechanical reliability even when damaged. Furthermore, using the fracture energy (Gc) calculation method developed by Greensmith, the Gc of the WPU elastomer was determined to be 146.57 kJ m^{-2} (Fig. 2e).

As shown in Fig. 2f, after 3 h of repair, the scratches on the surface of the WPU almost completely disappeared without leaving any traces, indicating its excellent scratch repair ability. The previously cut section on the sample underwent complete healing. Consequently, the regenerated elastomer exhibited remarkable properties, as it could be stretched to ~600% strain without any propagation of the original notch (Fig. 2g and Supplementary Movie 2). The above phenomenon, combined with FT-IR, indicated that during the room temperature repair process, the self-healing process of the WPU polymer chain at the cross-section was influenced by the following two factors: the secondary binding of the broken hydrogen bond, and the diffusion motion of the polymer chain on the cross-section.

Figure 2h shows the stress–strain curve of WPU repaired at 50 °C at different times. As the time increased, the self-healing efficiency of WPU gradually increased. When the repairing time was 12 h, the tensile curve of WPU was almost identical to before failure, indicating that it can fully repair its mechanical properties. The toughness of our work was as high as 300 MJ m^{-3}, which outperformed other room-temperature self-healable materials recorded in previous literature (Supplementary Table 1 and Fig. 2i)[27–31].

Characterization analysis of GO and coatings

Figure 3a shows the digital image of the fracture surface of GO film. The illustration on the upper right showed the low-resolution SEM image of GO, and the illustration on the lower right showed GO after rough grinding. The completely dried GO had certain candidates and ductility, which all indicated that GO was compact and smooth with layers stacked, and was an ideal filler. The microstructure of GO nanosheets was further observed using AFM and their layer thickness was tested. As shown in Fig. 3b, GO nanosheets had a typical two-dimensional layered structure. Meanwhile, according to the selected height map, the average thickness of GO nanosheets was 2.43 nm, indicating that the peeled nanosheets had a thickness of ~7 layers of C–N. The UV spectra of GO are shown in Fig. 3c. In Fig. 3c, GO exhibited two characteristic peaks, located at 232 and 299 nm, respectively,

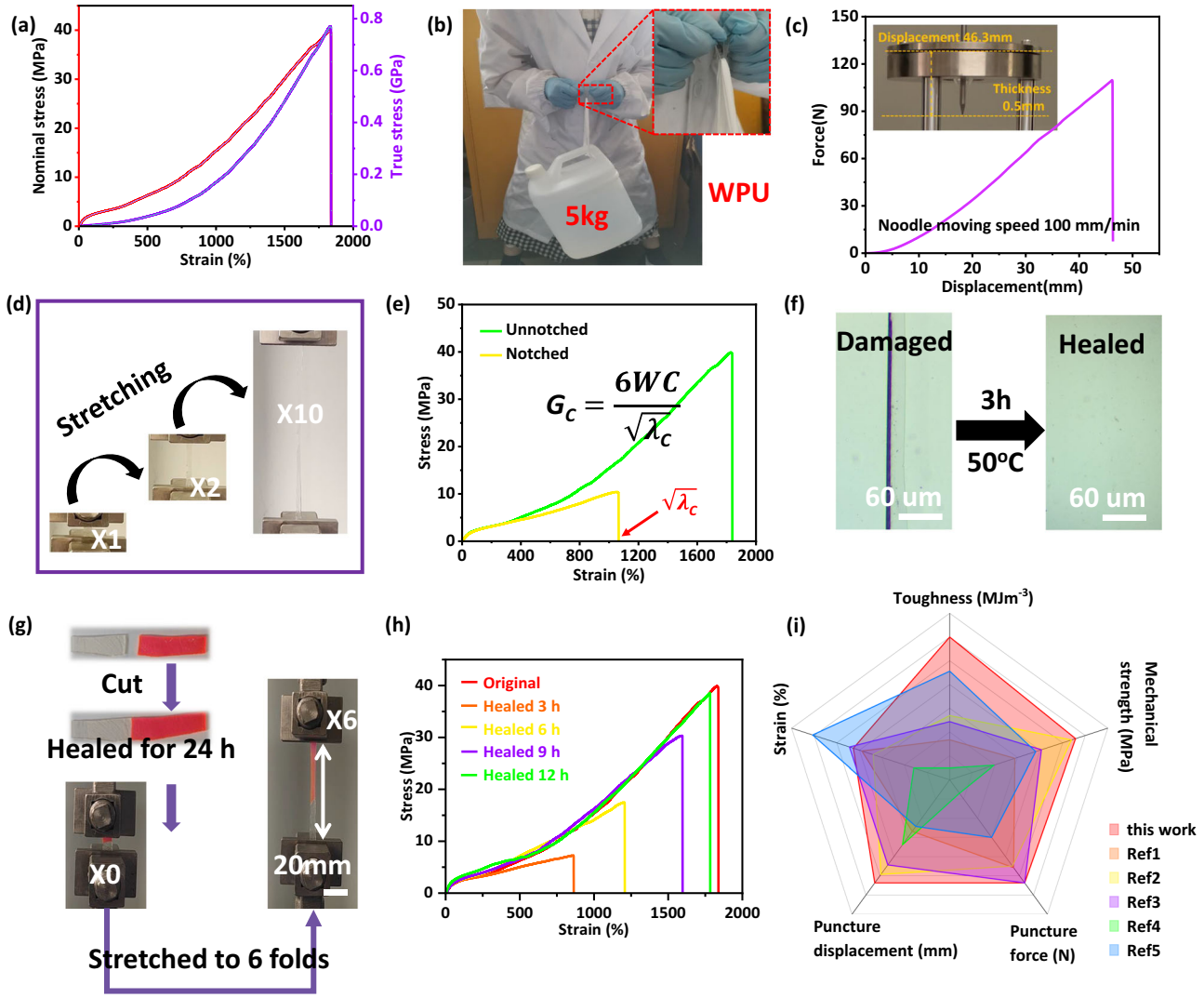

Fig. 2 Mechanical and self-healing properties of WPU materials. a Typical nominal (red) and true (purple) stress–strain curves of the WPU film. **b** Digital photographs of the 5.0 kg that the prepared WPU could withstand. **c** Force–displacement curve of the WPU elastomer with a thickness of ~0.8 mm, where the inset digital photograph showed the puncture resistance of the WPU. **d** Digital photographs of the notched WPU that was elongated to different strains. **e** Nominal stress–strain curves of the unnotched and notched WPU elastomers. **f** OM demonstrating the self-healing performance of the WPU film. **g** Photographs of the healed WPU specimen that could be stretched to 10-fold after only 10 min healing. **h** Typical stress–strain curves of the original and healed WPU for different healing periods at 50 °C. **i** Comparison of strain, toughness, mechanical strength, puncture force, and puncture displacement between WPU elastomer and other tough and healable polymers reported in previous works of literature (Supplementary Table 1).

mainly attributed to the π–π* transition of the C–C bond in the aromatic group and the n–π* transition of the C=O bond[32,33].

To verify the corrosion inhibition effect of GO, the Nyquist and bode plots of Q235 carbon steel in 3.5 wt% NaCl and 3.5 wt% NaCl + 0.5 mg ml^{-1} GO solutions were shown. From Supplementary Fig. 2, it could be seen that the Nyquist plot of Q235 carbon steel in a 3.5 wt% NaCl solution showed a smaller radius of the capacitive arc, while the radius of the capacitive arc increased in solutions containing GO. This may be because GO molecules would adsorb on the surface of carbon steel. The surface effect of GO increased the roughness of the carbon steel surface, to some extent preventing the direct contact between the metal surface and water molecules, thus delaying the process of corrosive ions penetrating the metal surface in the solution.

From the SEM image (presented in the left side of Fig. 3d) of the thin film formed after the drying of GO aqueous solution, it could be seen that the deposited film surface had a transparent layered structure and wavy folds, which was completely different from the morphology of large-scale stacked Gr powder (presented in the upper left corner of Fig. 3d), indicating that the prepared GO nanosheets had the advantages of more regular morphology and easy arrangement. Figure 3d overall presents the preparation process of WPU coating mixed GO. The GO nanosheets prepared by the modified hummers method were uniformly dispersed in WPU with excess solvent removed according to mass ratio. A coating preparation device of a bar coater was used to roll-coat on the Q235 carbon steel plate. The cartoon diagram in the illustration showed the brief preparation process of WPU/GO coating. In addition, it was also rolled onto white paper, and the illustration (presented in the upper right corner of Fig. 3d) showed a uniformly dispersed WPU/GO composite coating. The illustration at the lower right corner of Fig. 3d showed the optical microscopic (OM) images of WPU and WPU–GO lamellar structural (WPU–GOLM) coatings. It can be seen that compared to WPU polymers, WPU–GOLM films exhibited an opaque state, which was due to the addition of black GO slurry.

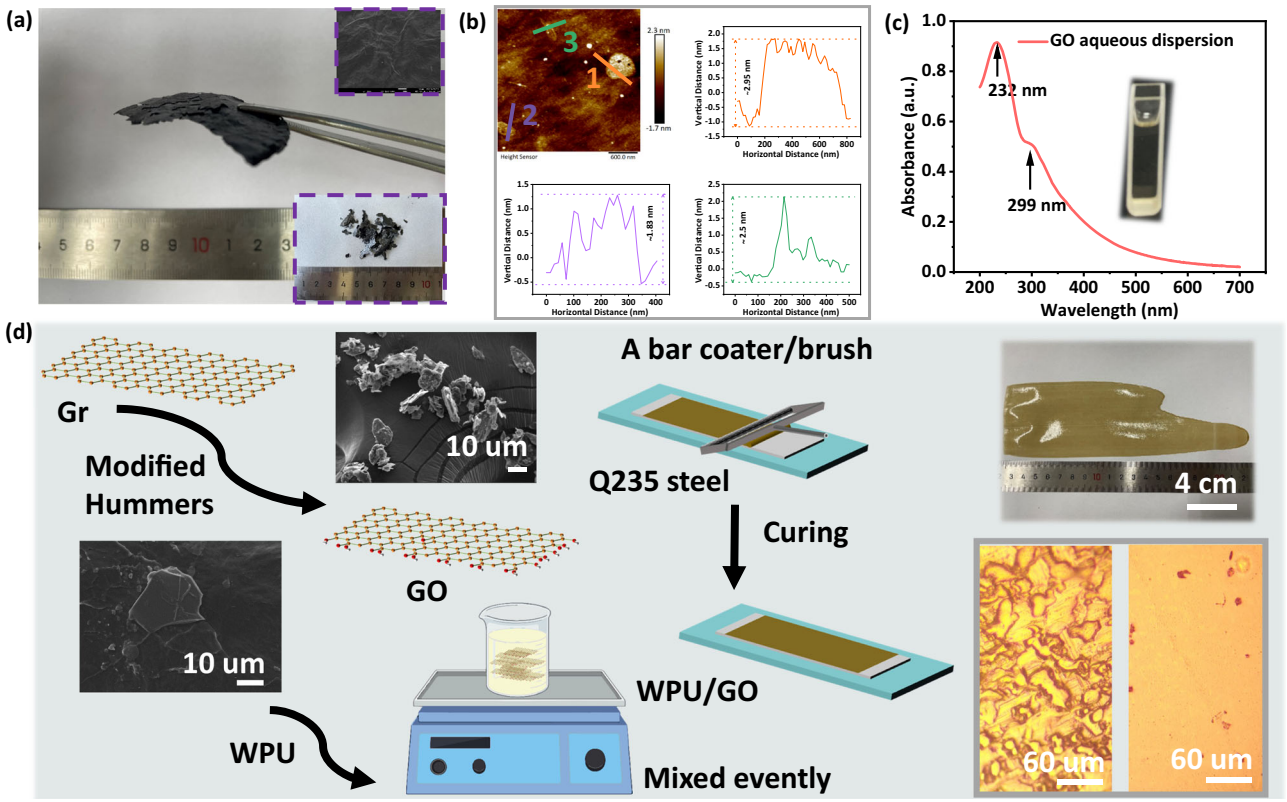

Fig. 3 Characterization of GO and preparation process of coatings. a The cross-section fracture morphology of the GO film. The SEM and digital photographs of the surface of the GO film are in the illustration. **b** AFM of the prepared GO and the corresponding height map of the selected area. **c** Absorbance of the GO aqueous dispersion. **d** The whole preparation route of coatings. The illustrations were respectively bulk Gr, GO, and the WPU-GO film on white paper, and the OM pictures of WPU and WPU-GOLM coating.

The incorporation of GO nanosheets in WPU–GO coatings led to an increase in interface and solid content. This, in turn, the viscosity of the coatings enhanced by restricting the movement of molecular chains, allowing them to maintain their shape after roller coating[26]. During the roller coating process at a speed of 150 mm s^{-1}, with high-precision coating rod gaps of ~15 μm, the larger lateral size of GO exerted a strong shear effect and imposed high-volume constraints on the viscous WPU–GO coating. As a result, the GO nanosheets align along the casting direction, leading to a flattened orientation of GO in the film (Fig. 4a)[34].

The ATR-FTIR spectra of the WPU are shown in Fig. 4b. The band at 3348 cm^{-1} was assigned to the N–H stretching vibration of urethane. The bands at 2931 and 2858 cm^{-1}, which corresponded to the C–H stretching vibration of $–CH_2–$ and $–CH_3$, respectively. Additionally, characteristic bands for polyurethane were also detected including those at 1523 cm^{-1} (N–H, bending vibration), 1454 cm^{-1} ($–CH_2–$, bending vibration), 1353 and 1423 cm^{-1} ($–CH_3$, asymmetric bending vibration, and symmetrical bending), 1230 cm^{-1} (C–O stretching vibration). The band at 1724 cm^{-1} was assigned to C=O. The above results indicated that the WPU polymer had been successfully synthesized. The chemical structure of the WPU polymer was also characterized by ^1H NMR (Supplementary Fig. 3). The Chemical shift of 5.84 ppm belonged to the characteristic peak of hydrogen on the nitrogen atom of Carbamate (–NH–CO–O–). The 4.37 and 4.19 ppm belonged to the characteristic peaks of hydrogen on urea-based (–NH–CO–N–) nitrogen atoms[8].

Furthermore, upon observing Fig. 4c, it was evident that GO presented four characteristic peaks at 1048, 1622, 1722, and 3422 cm^{-1} [19]. These peaks could be attributed to specific vibrations: epoxy C–O–C vibration, C=C skeletal vibrations from unoxidized graphitic domains, C=O stretching of carboxyl, and O–H stretching of hydroxyl, respectively[32,35]. The infrared peak of GO at 1622 cm^{-1} also existed in WPU–GO, but there was no such peak in WPU, indicating the successful preparation of WPU–GO materials. In addition, From Supplementary Fig. 4a, b, the peak at –NH significantly enhanced and shifted from 3373 to 3359 cm^{-1}. More importantly, the characteristic peak at 1727 cm^{-1} in WPU moved to 1723 cm^{-1}, and a supermolecule hydrogen bond was formed between GO and WPU on this surface. From the cross-sectional SEM of Fig. 4d, it could be seen that there was no significant difference in the thickness of the three coatings, which were ~52, 53, and 53 μm, respectively.

Anti-corrosion capability using EIS

EIS can provide a non-destructive method for assessing the anti-corrosion performance of WPU coatings within a specific time frame. During the EIS test at 25 °C, the corrosion behavior of the coating sample in a 3.5 wt% NaCl solution at pH = 7 for 2, 4, 6, 8, and 10 days was regularly recorded. Figure 5 illustrates the Nyquist and bode plots of WPU, WPU–GO random structural (WPU–GORM), and WPU–GOLM coatings.

In the Nyquist diagram, the capacitive arc represented the charge transfer resistance, and its magnitude reflected the corrosion rate[13]. The larger the radius, the more stable the performance of the coating layer and the better its corrosion resistance. From Nyquist plots of Supplementary Fig. 5a–c, it could be seen that as the soaking time prolonged, the capacitance reactance radii of the three kinds of coatings gradually decreased. Based on the size of the radii, the corrosion resistance of WPU–GOLM coating was significantly better than that of WPU–GORM and WPU coatings.

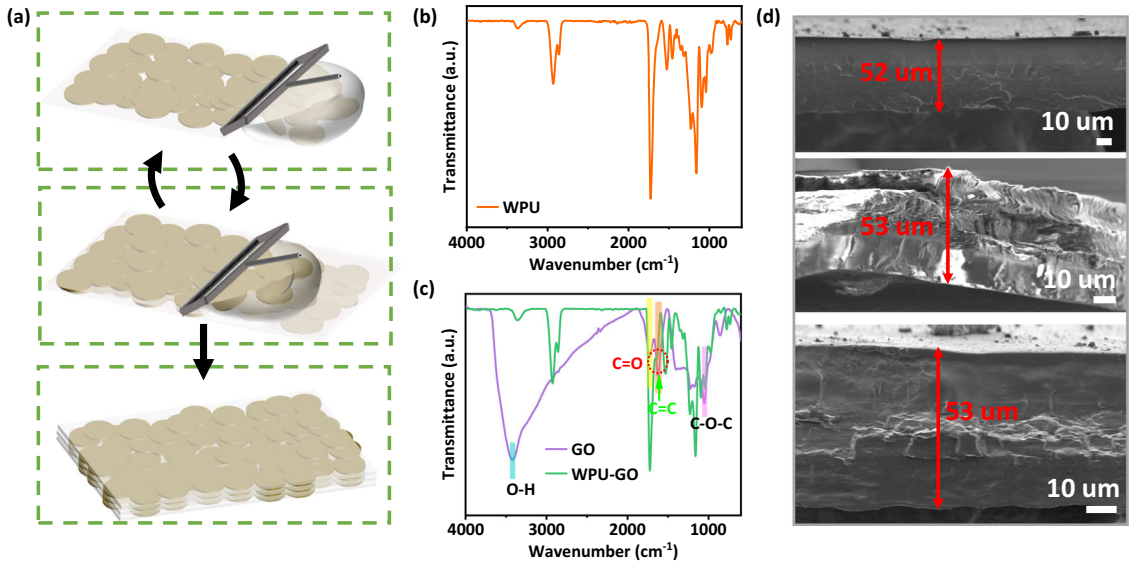

Fig. 4 Schematic illustration of WPU–GOLM coatings. a Diagram of preparation for WPU–GOLM coating with flat-oriented GO through the roll-coating method. **b** and **c** FTIR of GO, WPU, and WPU–GO materials. **d** The cross-section of the prepared WPU, WPU–GOLM, and WPU–GORM coatings (from top to bottom).

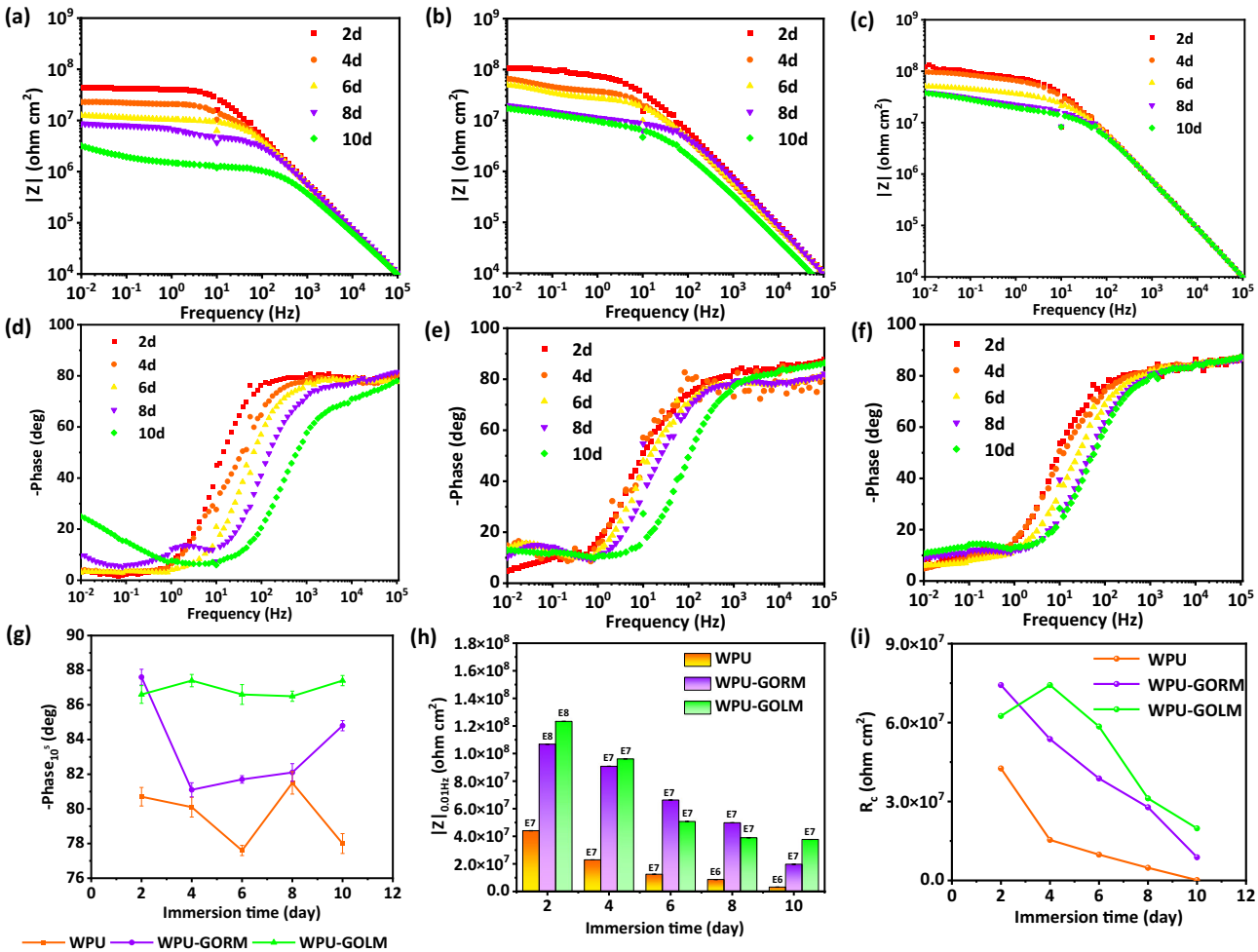

Fig. 5 EIS results of different coatings in 3.5 wt% NaCl solution. Bode-mode and bode-phase diagrams of **a**, **d** WPU coating, **b**, **e** WPU–GORM coating and **c**, **f** WPU–GOLM coating during immersion. **g** The high-frequency phase angle of different coatings during immersion. (mean ± standard deviation). **h** Low-frequency modulus of different coatings during immersion. (mean ± standard deviation). **i** Evolution of R_c value of reference and composite coating with immersion time. (mean ± standard deviation).

Moreover, an ideal surface coating should exhibit a high-frequency phase angle of −90°, which indicates that the coating is a nonconductive capacitor. As shown in Fig. 5g, during the soaking cycle, the WPU coating was not satisfactory, with a high-frequency phase angle of only 80.7 ± 0.535° during the initial soaking period. After 10 days of soaking, it decreased to 78 ± 0.572°. Unlike this, the phase angles of WPU–GOLM coating at high frequencies were stable at 86.5 ± 0.294°–87.4 ± 0.294°, close to 90°, indicating that they had good capacitance characteristics. Overall, these results indicated that the WPU–GOLM coating exhibited excellent barrier performance in its intact state[36]. At the same time, although the phase angle of WPU–GORM coating was not maintained as stable as that of WPU–GOLM coating, it was also higher than that of WPU coating.

The impedance mode value at 0.01 Hz ($|Z|_{0.01Hz}$) in the bode-mode diagram can be utilized as a semi-quantitative measure to evaluate the barrier performance of coatings[37]. The higher $|Z|_{0.01Hz}$, the better the corrosion resistance of the material. As shown in Fig. 5a–c, all coatings exhibited similar electrochemical behavior, with $|Z|_{0.01Hz}$ values gradually decreasing with increasing immersion time. Especially for WPU coating, the $|Z|_{0.01Hz}$ starting from 4.405×10^7 ohm cm^2 (2 days) dropped to 3.191×10^6 ohm cm^2 (10 days) indicating that the corrosion resistance of this coating was approaching a failure. Figure 5h visually displayed the variation patterns of $|Z|_{0.01Hz}$ for the three different coatings. In contrast, during the initial soaking period, the $|Z|_{0.01Hz}$ values of WPU–GORM and WPU–GOLM coatings were as high as 1.068×10^8 and 1.233×10^8 ohm cm^2, respectively, all higher than WPU coating. After soaking for 10 days, the WPU–GOLM coating still maintained a high level and remained stable at 3.771×10^7 ohm cm^2, showing the highest protective ability, increased by ~1.0 orders of magnitude compared to WPU coating. These above results confirmed that the barrier anti-corrosion performance of WPU coating had been improved in the presence of well-dispersed GO nanosheets[14]. In addition, the enhancement of the protective efficiency (PE%) of WPU coatings with higher orientation added by GO nanosheets was evaluated using Eq. (1) [33].

$$PE\% = \frac{|Z|_{0.01Hz} - |Z^*|_{0.01Hz}}{|Z|_{0.01Hz}} \times 100\% \quad (1)$$

In Eq. (2), $|Z|_{0.01Hz}$ and $|Z^*|_{0.01Hz}$ are the low-frequency impedance values of the coating with GO and the coating with pure WPU soaked for 10 days, respectively. Compared with the blank control sample, the PE values of the WPU–GORM and WPU–GOLM samples were 58.8% and 74.2%, respectively. These results indicated that GO with a higher orientation degree could better ameliorate the barrier/activity inhibition performances of WPU coatings.

To further examine the corrosion behavior of these WPU coatings, impedance data was interpreted using an equivalent circuit model (Supplementary Fig. 6a–e) to explain the evolution process. The circuit model included solution resistance (R_s), coating resistance (R_c), coating capacitance (CPE_c), charge transfer resistance (R_{ct}), double-layer capacitance (CPE_{dl}), and Warburg impedance (Z_w). The impedance Z_w represented the diffusion resistance caused by the ion exchange process. To achieve better fitting results, constant phase elements (CPE) were used instead of pure capacitive components during the fitting process. Here, CPE represented a constant phase element, which described the non-ideal capacitive response caused by surface non-uniformity. The fitting parameter C represented the CPE_{dl} in our case.

From the Nyquist of WPU (Supplementary Fig. 5a), it could be seen that during the initial soaking period (2 days), a semicircular arc along with a trailing end appeared. At this point, two-time constants were displayed, this meant that the corrosive electrolytes gradually reached the metal surface. At this time, the corresponding equivalent circuit model of the coating was shown in Supplementary Fig. 6a. Supplementary Fig. 5d was an enlarged version of Supplementary Fig. 5a. Combining the Nyquist plot and bode-phase plot, it could be seen that with the passage of soaking time (8 days), the coating appeared two capacitive arcs with a diffusion tail. At this point, the diffusion process appeared near the steel electrode, indicating a period of severe metal corrosion. The diffusion behavior of cathodic reactions can be revealed through Z_w. The control step of the corrosion reaction had been converted from coating resistance to charge transfer resistance, and the mass transfer process could be demonstrated by the circuit in Supplementary Fig. 6e. Due to the presence of micropores and microcracks in the coating matrix, the WPU coating quickly reached its saturation state.

The evolution processes of WPU–GORM and WPU–GOLM coating were similar to that of WPU coating in the early stage. The capacitance radius gradually decreased with immersion time increasing, this meant that a portion of the corrosive medium had entered the interface between the metal substrate and the coating. Since some water and electrolytes entered the interface between the coating and the metal, causing some corrosion products. However, owing to the physical barrier effect of GO, the WPU–GORM and WPU–GOLM coating could still maintain its state after the later stage of soaking, without significant diffusion. More importantly, for composite coatings, the reduction in capacitance radius was to some extent suppressed. During the whole immersion process, these two coatings showed an electrochemical process with two-time constants, and the fitting circuits were Supplementary Fig. 6a–d.

As the soaking process progressed, the fitting values of these components underwent a series of changes. To illustrate the changes in barrier function and anti-corrosion performance of coatings during immersion, R_c is commonly used to measure the physical barrier of coatings[38]. Therefore, we would focus on the evolution of R_c (Fig. 5i). Overall, the R_c of all coatings showed a decreasing trend with the prolongation of soaking time. Among them, the R_c values of WPU and WPU–GORM coatings were relatively low throughout the entire soaking process. While the R_c values of WPU–GOLM coatings were higher, indicating strong physical shielding performance[13]. From Supplementary Table 2, it could be seen that contrary to the tendency of R_c, Q_c showed an upward trend with the extension of soaking time. A coating system with excellent protective performance will exhibit higher R_c and lower Q_c values. Compared with WPU coating, both coatings added with GO had relatively higher R_c values and lower Q_c values[39]. Among all coatings, the WPU–GOLM coating exhibited the lowest Q_c value, indicating that under the roller coating process, the lamellar GO could effectively suppress electrochemical reactions occurring at the metal/coating interface. Furthermore, the R_{ct} value of WPU–GOLM coating was $1.581 \times 10^7 \pm 7.995 \times 10^1$ ohm cm^2 (WPU–GORM coating was $1.172 \times 10^7 \pm 2.005 \times 10^2$ ohm cm^2), greater than the value of WPU ($5.659 \times 10^5 \pm 3.103 \times 10^1$ ohm cm^2). The WPU–GOLM coating had better anti-corrosion properties than the WPU coating. It also indicated that the prepared GO did not possess "corrosion-promoting activity"[40].

It is generally believed that the order of magnitude of coatings with low-frequency modulus values >6 still have protective capabilities. Therefore, at this time, all three coatings after 10 days also had certain anti-corrosion properties. The reason why GO-based WPU polymer coatings had better anti-corrosion performance than WPU could be explained in this way. One reason may be that the interface hydrogen bond formed between the active site on WPU and GO played a role in sacrificing the hydrogen bond, which could effectively dissipate external energy[41]. Thus, the fracture toughness of the composite coating was improved, and the corrosive medium could be further prevented from propagating to the coating interface through cracks. The better

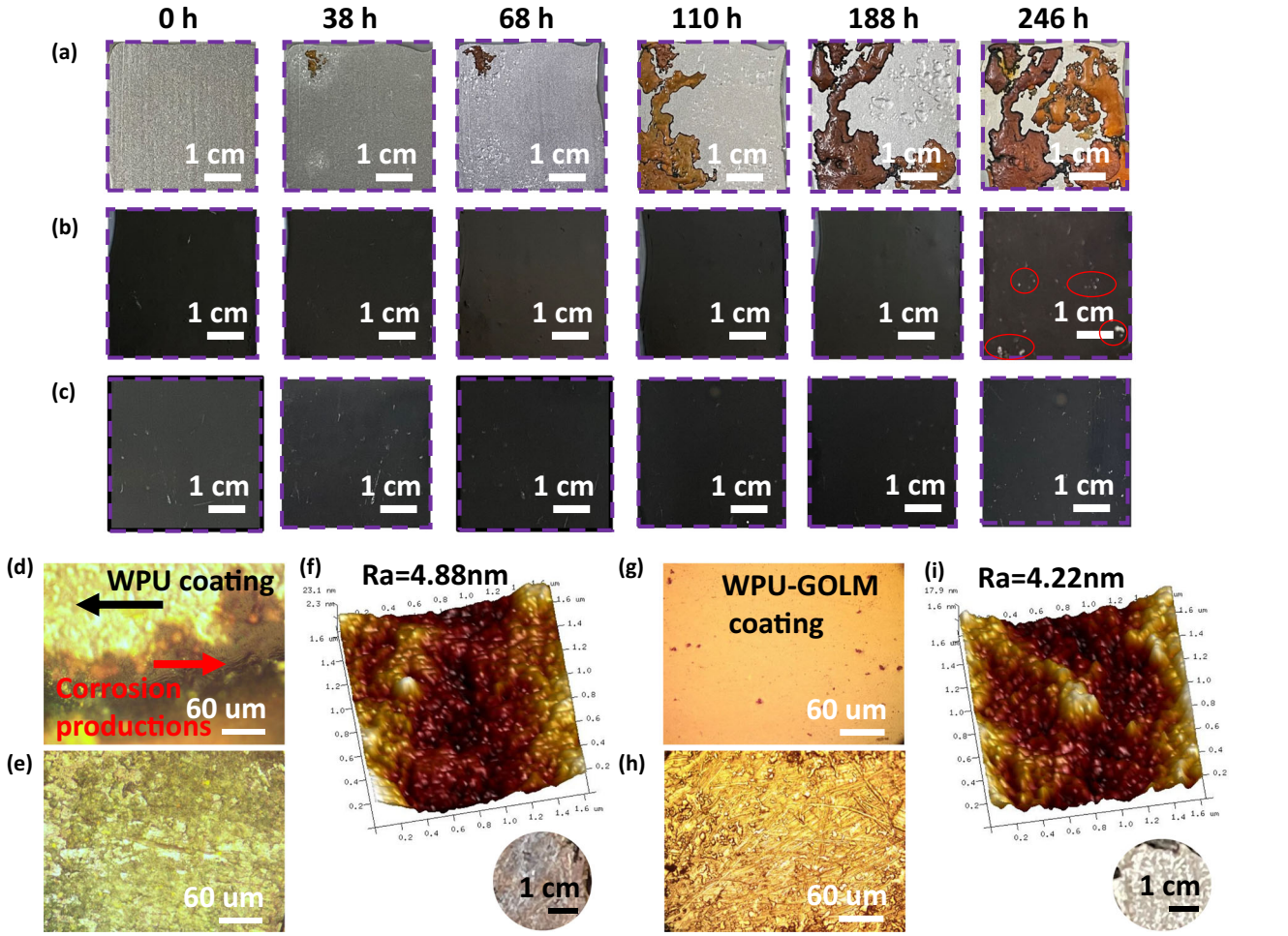

Fig. 6 Analysis of large-scale immersion test in 5.0 wt% NaCl solution. Digital images of **a** WPU, **b** WPU–GORM, and **c** WPU–GOLM coatings immersed in 5.0 wt% NaCl solution at different times. OM of the **d** WPU coating and **g** WPU–GOLM coating surface soaked for 246 h and **e**, **h** the corresponding carbon steel with the coating removed. AFM images of the **f** WPU coating and **i** WPU–GOLM coating surface morphology and digital photos of the corresponding carbon steel with the coating removed (inset in the lower right corner).

anti-corrosion reason for WPU–GOLM was that the parallel arrangement of GO improved the corrosion resistance of WPU–GOLM coatings more efficiently[18]. In Supplementary Table 3, from three perspectives of coating thickness, soaking time, and low-frequency modulus, we also compared the anti-corrosion performance of coatings in other literature. Under the same conditions, the coating we prepared had a better performance[8,33,41–43].

Large area simulated seawater immersion tests and corrosion product analysis

Long soaking tests can more intuitively display the anti-corrosion property of the coating. Unlike the EIS test sample, the larger area (4 cm × 4 cm) of the coating was exposed to the 5.0 wt% NaCl solution. It could be seen that as the soaking time increased, each coating exhibited varying degrees of corrosion. However, compared to the EIS results, the WPU-coated carbon steel plate was unbearable, compared to the other two coated plates. In terms of segmentation, after soaking for 38 h, the WPU coating showed blistering and deposition of yellow-brown corrosion products. After 246 h, a large area of corrosion products showed that the WPU coating had been completely penetrated by the corrosive medium, and the coating had failed. On the other hand, the soaking time lasted until 188 h, and due to the presence of large-scale two-dimensional GO nanosheets, both WPU–GORM and WPU–GOLM had good corrosion protection performance[44]. It was not until the soaking time was 246 h that pitting corrosion appeared on the surface of the WPU–GORM coating, but the coating did not show blistering or peeling. Most importantly, the WPU–GOLM coating did not exhibit any corrosion phenomenon after soaking for 246 h.

To further verify the effectiveness of coating protection, OM technology was adopted to inspect the micro-morphology of the coating after stripping the metal substrate. Figure 6d–i shows the surface morphology of WPU and WPU–GOLM coatings after soaking for 246 h. From the OM image, it could be seen that the surface of the WPU coating consisted of a large amount of yellow-brown corrosion products (Fig. 6d), while the surface of the WPU–GOLM coating was intact and free of corrosion products (Fig. 6g). In addition, the AFM diagram showed the surface roughness of the bare steel after soaking and removing the coating. The surface roughness of carbon steel with the WPU–GOLM coating removed was 4.22 nm (Fig. 6i), which was smaller than that of carbon steel with the WPU coating removed. Compared with the EIS analysis data, WPU and the other two coatings were more intuitive to simulate immersion in large areas of seawater for a long time. The WPU comparison was terrible, no matter how it compared to either WPU–GORM or WPU–GOLM coating.

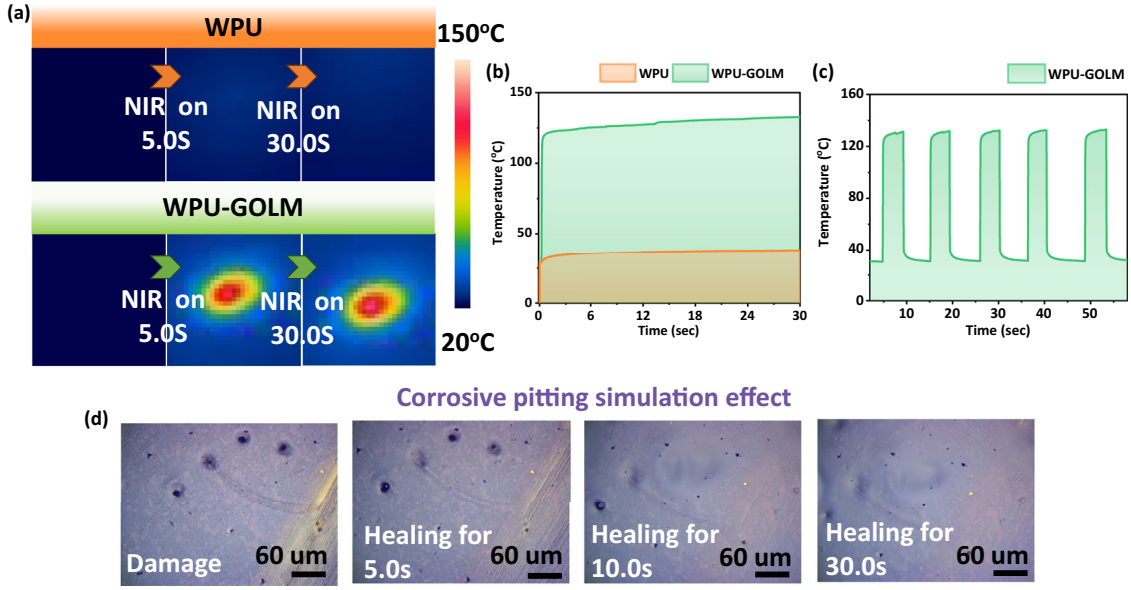

Fig. 7 NIR-triggered healing performance of the WPU–GOLM coatings. a Time-dependent infrared thermal FT-IR images and **b** the corresponding photothermal heating curves of WPU and WPU–GOLM irradiated. **c** Cyclic heating and cooling curves of WPU–GOLM coating. **d** OM pictures of the WPU–GOLM coating healed under NIR laser irradiation at 1.0 W cm^{-2}.

NIR-light response self-healing performance of WPU–GOLM coatings

Supplementary Fig. 7 revealed the WPU–GOLM coating could achieve self-healing under heating conditions. However, when self-healing materials are mixed with other polymer-based products, if there are materials near self-healing material that cannot withstand higher temperatures, then self-healing material cannot achieve a hotfix. Light stimulation repair offered the advantage of precise, remote, and timely irradiation specifically targeting damaged areas, without interference from unrelated regions[43]. GO enhanced the potential of light stimulation repair in materials due to its excellent NIR absorption capability. To confirm the photo-thermal conversion efficiency of GO, the surfaces of WPU and WPU–GOLM coatings were exposed to a modulated fiber-guided NIR laser (808 nm). The changes in their surface temperatures were recorded with an infrared thermographic camera. The experimental results are shown in Fig. 7a. For the WPU–GOLM coating, after 5.0 s of NIR laser irradiation, the surface temperature rapidly increased to 124.75 °C. After 30 s of irradiation, the surface temperature could reach 132.8 °C. When the NIR laser was shone on the surface, GO arranged in parallel in the WPU would quickly respond and convert into thermal energy. On the contrary, the WPU coating showed almost no temperature change under the same conditions and period. This indicated that the WPU–GOLM coating had a high photothermal conversion efficiency. In addition, all heat source response areas were limited to luminous components, providing an effective method for accurately repairing damaged materials.

The coating was subjected to NIR laser irradiation at intervals to further verify the thermal conductivity of the WPU–GOLM coating. As shown in Fig. 7c, under an irradiation time of 5.02 s, the temperature rose to 124.7 °C. And the coating was continued to be irradiated for 9.3 s, the temperature reached 131.4 °C. After immediately turning off the laser, the temperature immediately dropped to 62.0 °C (9.34 s), and after 9.5 s, it dropped to 37.6 °C. Five cycle tests (Fig. 7c) confirmed that the WPU–GOLM coating had good thermal conductivity and photothermal conversion efficiency. And this performance precisely brought excellent NIR-triggered healing ability to the material.

Under NIR laser irradiation, the coating was healed for 30.0 s (Fig. 7d). As time went on, the four holes on the coating surface gradually disappeared. It can be seen that under the irradiation time of 5.0 s, the small hole had been repaired. At 10.0 s, the two mesopores on the coating disappeared. At 30.0 s, the largest hole in the coating was completely repaired. Overall, our WPU–GOLM coating achieved optical healing in a short period of 30.0 s, making ultra-fast repair of damaged materials a reality. This simulated pitting repair test provided important insights into the field of NIR efficient self-healing and anti-corrosion.

Evaluation of anti-corrosion and self-healing capacity using SVET

Figure 8 shows the in-situ monitoring results of SVET for WPU with artificial defects, WPU–GORM, and WPU–GOLM coating/carbon steel systems immersed in a 3.5 wt% NaCl solution for different times. This reflected the distribution of corrosion current at the coating/carbon steel interface[45]. By prolonging the soaking time, the maximum anodic corrosion current density caused by WPU coating defects increased from 16 to 27 μA cm^2. This indicated that the carbon steel at the WPU-coating defect gradually dissolved and the corrosion became increasingly severe. When the soaking time was 14 h, the anodic corrosion current slightly decreased to 24 μA cm^2, but at this time, the cathodic corrosion current density reached 8 μA cm^2. This indicated that the continuously dissolved anode had transformed into a cathode of consuming oxygen. The cathode area that slowly expanded outward was the prerequisite for coating detachment. On the other hand, after soaking for 2 h, the maximum anodic corrosion current density of the WPU–GORM coating was 11 μA cm^2. The time was extended to 7 h and increased to 16 μA cm^2, at which point a cathodic corrosion current density of 1 μA cm^2 was generated. The anodic corrosion current density after 14 h was 24 μA cm^2, which was consistent with WPU, but it was worth noting that the cathodic corrosion current density disappeared at this time. Correspondingly, the WPU–GOLM coating showed a slight increase in maximum anodic corrosion current density from 8.8 to 9 μA cm^2, with no significant increase. After 14 h, the maximum anodic corrosion current density increased to 14 μA cm^2, at this point, the cathodic corrosion current density

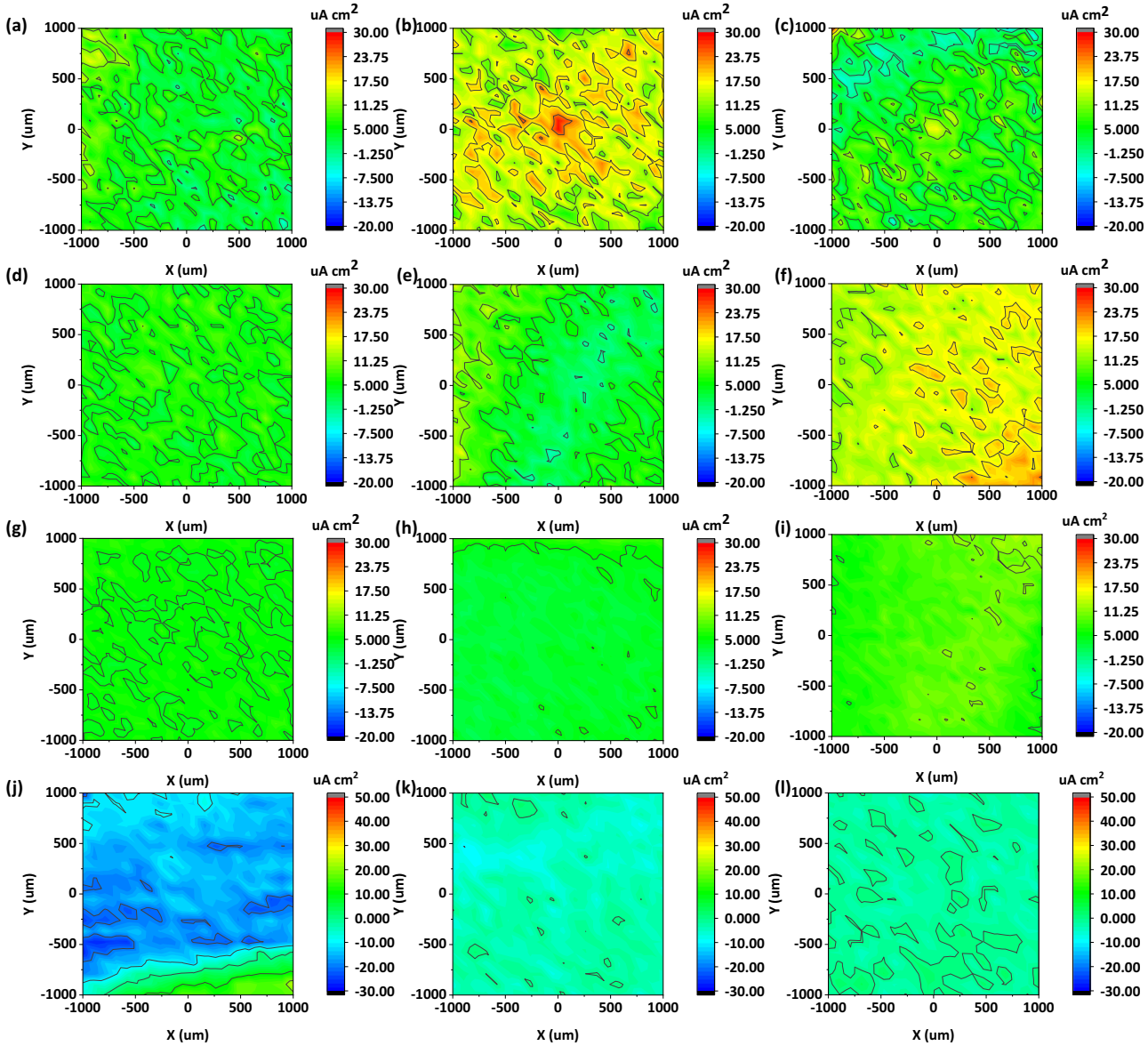

Fig. 8 SVET results of different coatings in 3.5 wt% NaCl solution. SVET current density maps of **a–c** the WPU coating, **d–f** WPU–GORM coating, and **g–i** WPU–GOLM coating immersed for 2, 7, and 14 h, respectively. **j** The WPU coating was immersed for 24 h and it was immersed again after being heated at 60 °C for 6 h for **k** 1 and **l** 24 h, respectively.

had not yet appeared. Judging from the maximum anodic corrosion current density, both WPU–GORM and WPU–GOLM coatings were superior to WPU coatings. Judging from the cathodic corrosion current density, although the WPU coatings did not exhibit a significant cathodic current density, it was relatively larger compared to the other two. Therefore, from the perspective of SVET, it also indicated that GO uniformly dispersed in the polymer could improve the barrier performance of the original coating[36].

To evaluate the self-healing capability of WPU coatings again, considering that the current density of WPU coatings after soaking for 14 h was not very high (Fig. 8a–c), we extended the time to 24 h in the later operation to see if the current density would increase at this time, to better demonstrate. As expected, the WPU samples soaked for 24 h showed higher anode and cathode current density (Fig. 8j). After the coating was placed at 60 °C for 6 h, the current situation was monitored again. It could be observed that the anode current density and cathode current density significantly decreased at this time (Fig. 8k). After soaking for 24 h, there was no significant fluctuation in current density and it was close to the noise level, indicating that the WPU coating was completely repaired (Fig. 8l).

Protection mechanism of the coating

One of the main reinforcing points of fillers/polymer composites is the dispersibility of nanosheets in the polymer matrix[46]. Therefore, it is an important node to overcome the Van der Waals force between GO layers to avoid the agglomeration of nanosheets in the polymer matrix. As is well known, the changes in ζ potential values are closely related to the stability of dispersions. The stability of the dispersion is usually judged by the absolute value of ζ potential[47]. Generally speaking, if the absolute value of ζ potential is >30 mV, it means that the entire dispersion system is relatively stable[48]. The larger the value, the more stable the system. More importantly, understanding the surface charge on

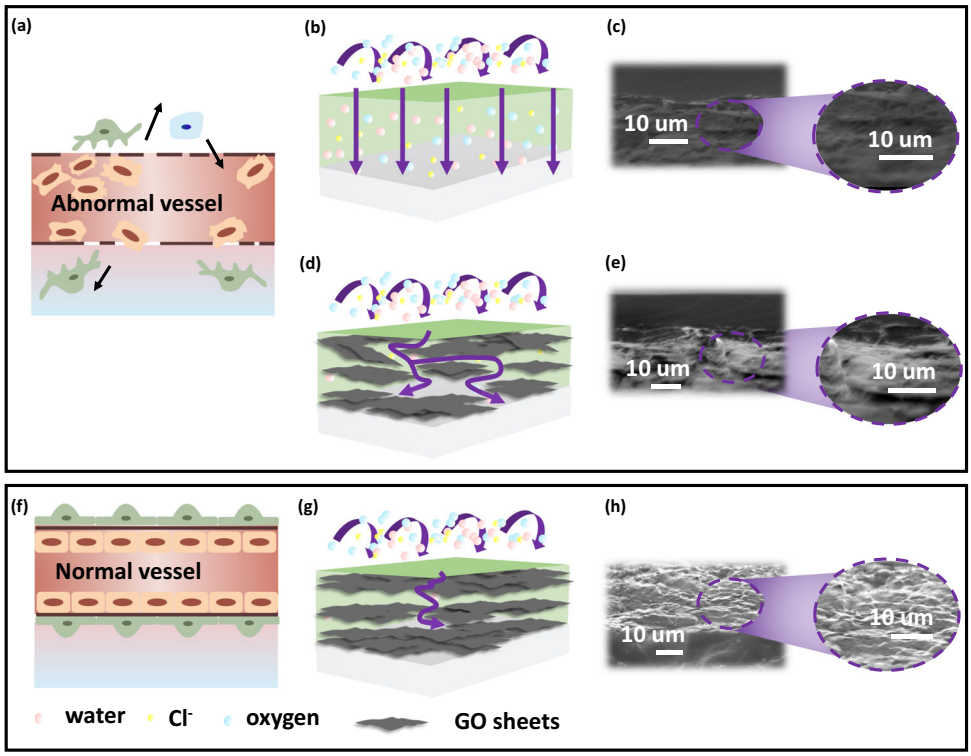

Fig. 9 Anti-corrosion mechanism of biomimetic coatings. Schematic of the mechanism of the anti-corrosion performance of WPU **a**, **b**, WPU–GORM **a**, **d**, and WPU–GOLM **f**, **g** composite coatings. **c**, **e**, **h** SEM images of the fracture cross-section of WPU, WPU–GORM, and WPU–GOLM composite coatings.

GO was important to explain their influence on the ion resistance of WPU coating. Hence, at pH = 7, the GO nanosheets were measured ζ potential value. It can be seen from Supplementary Fig. 8 that the ζ potential value of GO aqueous dispersion was −33.7 ± 1.283 mV, indicating that the dispersion was sufficiently stable. The ζ of WPU–GO composite aqueous dispersion became higher (−39.9 ± 0.860 mV). That indicated that WPU lotion could give GO dispersion a higher negative charge value, and the absolute value was more than 30 mV, indicating that the stability of WPU–GO dispersion was relatively stable[41].

Figure 9a shows a schematic diagram of incomplete blood vessels in tumor tissue, where cancer cells could easily enter and metastasize through the bloodstream. Figure 9f shows blood vessels in normal healthy tissues. Inspired by the mechanism of action between the human immune system and tumor blood vessels, we prepared a biologically inspired self-healing anti-corrosion coating.

When the coating was subjected to long-term erosion, local corrosion was inevitable[49]. In the anode region, the metal lost electrons and was oxidized, and the metal ions underwent hydrolysis, resulting in a decrease in the pH value of the anode region. In the cathode area, the electrons from O_2 were reduced to generate OH^-, which increased the local pH value. The increase of pH would cause more functional groups on the GO surface to be deprotonation, resulting in more negative charges and more negative ζ potential[50]. Therefore, GO with higher negative charges further affected the ion resistance of the coating[51]. In this scenario, the coating demonstrated a cationic selectivity phenomenon. Cl^- and OH^- were unable to diffuse into the coating until the coating charge became positive or neutral. Therefore, less corrosive Cl^- and OH^- ions could reach the coating/metal interface[52]. This was also one of the reasons why WPU–GORM and WPU–GOLM coatings could reduce the probability of hydrolysis degradation and adhesive performance damage.

Figure 9b, d shows the corrosion penetration process of WPU coatings without nanostructures and WPU coatings with randomly arranged GO under corrosive medium damage. Through the field emission SEM image (Fig. 9e) of the fracture surface of the coating, some GO nanosheets were not arranged in parallel orientation. In contrast, in Fig. 9h, it was observed that GO nanosheets as "bricks" exhibited a lamellar structure almost parallel to the metal matrix. This discovery indicated that GO, which was uniformly dispersed in the coating, had a high degree of orientation. This was mainly due to the presence of a large number of hydrogen bonding between WPU–GOLM, as well as the hydrogen bonding interaction between –COO– and –OH of the ultra-thin GO and WPU, caused GO to be parallel to the substrate and arranged between the coatings and promoted the occurrence of the self-alignment phenomenon[41]. Consequently, this approach enabled the achievement of a highly oriented dispersion of GO sheets and ensured strong bonding with the WPU matrix. In addition, the high specific surface area and impermeability to water, O_2, and ion diffusion of GO nanosheets created a long and tortuous permeation path for corrosive media while providing a good barrier effect (Fig. 9g). More importantly, this composite coating can avoid direct contact with the substrate, thereby shielding against galvanic corrosion[53]. Therefore, the biomimetic-inspired self-healing WPU–GOLM coating had better anti-corrosion efficiency.

The coatings were soaked in two solvents (ethanol and ethyl acetate), to evaluate the effect of organic solvents on the performance of the coating. According to Supplementary Fig. 9, it can be seen that the water contact angle of the coating was tested at different times. Although the water contact angle of the coating did not reach the superhydrophobic level, the change in contact angle before and after immersion was relatively small, indicating that the WPU–GOLM coating also had strong corrosion resistance to organic solvents[54]. Combined with immersion tests,

the WPU–GOLM coating we prepared exhibited excellent stability in both aqueous and organic solvents.

DISCUSSION

Here, we proposed a strategy for constructing a multi-functional biomimetic structural polymer material. It was mainly made by dispersing and integrating the polyurethane material with a fourfold cross-linked network of covalent bond, reversible hydrogen bond, ionic bond, and hydrophilic group in the main chain with GO nanosheets through non-covalent hydrogen bond at the interface. This highly oriented coating could be applied on different substrates by a roller coating process. Biomimetic materials obtained exhibited multiple dynamic bonds and highly oriented structures with dissociative and reconfigurable effects, exhibiting exciting self-healing properties. This approach not only endowed them with NIR-responsive self-healing function but also improved their anti-corrosion performance. To validate the efficacy and reliability of the WPU–GOLM coating as a protective layer for carbon steel, EIS, large-scale seawater simulation, and SVET experiments were conducted. The results strongly supported the suitability and dependability of the coating, and the corrosion product test outcomes provided robust evidence in favor of this argument. This study demonstrated the ability to confer self-healing capabilities on biomimetic materials through the selection of appropriate functional polymer chains and the careful optimization of coating processes. As such, it represented a universal method for preparing high-performance functional materials.

METHODS

Materials and chemistry

Gr powder (350 mesh) was purchased from Qingdao Huatai Lubrication and Sealing Technology Co., Ltd. Sulfuric acid (H_2SO_4, 37 wt%), potassium permanganate ($KMnO_4$), hydrogen peroxide solution (H_2O_2) hydrochloric acid (HCl, 37 wt%) and anhydrous ethanol were purchased from Drug Warehouse of Nanjing University of Science and Technology. Polycaprolactone diol (PCL, average $M_w \sim 2000$, CAS: 36890-68-3) was purchased from Shanghai Sigma-Aldrich Co., Ltd. Dicyclohexylmethylmethane-4 (HMDI, CAS: 5124-30-1) was purchased from Shanghai Adamas Co., Ltd. Dibutyltin dilaurate (DBTDL, catalyzer, CAS: 77-58-7), 2,2-Bis(hydroxymethyl)butyric acid (DMBA, as the hydrophilic chain-extender, CAS: 10097-02-6) were purchased from Shanghai Aladdin Biochemical Technology Co., Ltd. 4,6-Diaminopyrimidine (chain-extender, CAS: 2434-56-2), triethylamine (CAS: 121-44-8), rhodamine B, acetone and N, N-dimethylformamide (DMF) were purchased from Nanjing Nanshi Chemical Reagent Co., Ltd. Sodium chloride (NaCl, analytical purity). The water utilized in this work was deionized water with high purity. Q235 carbon steels were utilized as the substrates, which were purchased from Guangdong Honghong Industrial Co., Ltd. All chemical reagents were used directly without pretreatment.

Fabrication of WPU

Before the experiment, PCL and DMBA were put into a vacuum drying oven and dried in a vacuum for 10 h at 90 °C. Acetone and DMF were added to the 4 A molecular sieve to remove water. First, the system was set at 70 °C. The 5 g of PCL was added into a two-necked flask. Subsequently, 0.02 g of DBTDL catalyst and 1.88 g of HDMI, were diluted in acetone, and 0.444 g of hydrophilic chain extender DMBA were dissolved in DMF solution and added sequentially. The entire system was slowly heated to 80 °C and continuously stirred in a nitrogen atmosphere, followed by a reflux reaction for 4 and a half hours. The 0.165 g of 4,6-diaminopyrimidine dissolved in DMF and 0.01 g of DBTDL catalyst diluted with acetone were added in sequence. After 5 h of reaction, the system was cooled to 60 °C. After 17 h, 0.303 g triethylamine was added, and then slowly 15 ml water was added to emulsify. After the reaction lasted for about 3 h, the obtained product was placed on the rotary evaporator to evaporate acetone. The final polyurethane waterborne lotion was obtained and named WPU. In addition, to facilitate our research on the properties of the prepared polyurethane material, the preparation route is shown in Fig. 1a.

Fabrication of GO

The low-defective GO suspension was prepared by a modified Hummers' method[55]. For this aim, 46 ml of H_2SO_4 was taken into a beaker, which was stirred in an ice water bath at 200 rpm min^{-1}. After adding 1 g of Gr slowly, 3 g of $KMnO_4$ was slowly added into the system. The 4.6 ml of water was added after the temperature was dropped and continued to stir for 12 h. Next, 160 ml of water was poured into the system. The 10 ml of H_2O_2 was added until no bubbles were generated in the system. The product was filtered by suction with 3 wt% HCl solution, which was obtained by diluting with original HCl. Then, the filter cake was dissolved in 400 ml of water and stirred overnight. Afterward, the dispersion was poured into a dialysis bag ($M_w = 10{,}000$) for dialysis for 4 days. During the dialysis process, the water was changed every day. The final product obtained was recorded as GO dispersion.

Preparation of coating samples

The experimental samples were selected Q235 carbon steel as the substrate material. Before coating, the surface oxide layer was removed by manual polishing with 600 mesh and 1000 mesh sandpaper, and the surface was cleaned and dried with anhydrous ethanol for later use. A plasma instrument was used to perform surface hydrophilization treatment on Q235 carbon steel.

The 0.075 g of GO was weighed and dispersed in 2 ml of DMF solution and sonicated for 20 min. Then 3.69 g of WPU was added and stirred further for 2 min using a high-speed disperser at 2000 rpm min^{-1}. The hybrid WPU coating with embedded GO was kept in a vacuum to defoam. Then, roller coating equipment was used to roll the mixture onto the surface of the substrate. The obtained final intelligent composite material was called as WPU–GOLM coating. The proportion of GO filler added into WPU was 2.0 wt%. A similar method was used to prepare samples for comparative testing, except for using a brush as the tool (WPU–GORM coating). In addition, a blank control WPU coating was prepared using a route similar to the aforementioned WPU–GOLM coating. When making coating samples, it was necessary to wait until the surface of the previous coating reached surface drying (with a coating interval of about 12 h between each coat) before applying the second coat. The preparation process of the third layer of coating was consistent with the first two layers. The roller coating equipment used was a bar paint film preparation device (Guangzhou XinYi Laboratory Instruments Co., Ltd.), which could accurately control the wet film thickness. During the coating process, the coating thickness was controlled through roller coating equipment and weighing methods. The final coatings were cured at 80 °C for 24 h and placed for 7 days at room temperature to get dry films. Ultimately, the thickness of the coatings was approximately 50 ± 5 μm. The application of WPU and composite coatings follows GB/T 1727-2021[56]. The coated Q235 steel plates (150 mm × 70 mm × 2 mm) were utilized for EIS tests, immersion tests, and NIR self-healing tests. The coated Q235 steel plates (10 mm × 10 mm × 2 mm) were utilized for the anti-corrosion and self-healing performances of the SVET tests.

Mechanical tests of WPU polymers

The tensile performance test was conducted using Shimadzu's AGS-X tensile machine. The tensile specimens were standard ISO 37-3 dumbbell tensile specimens, and the average test results were obtained from three tests. The test temperature was 25 °C

and the tensile speed was 100 mm min^{-1}. The fracture toughness was calculated from the corresponding integral area below the tensile curve.

True stress (σ_{True}) at different strains was defined by considering a constant sample volume between the clamps. True stress (σ_n) was calculated according to the following Eq. (2):

$$\sigma_{True} = \sigma_n \times (\varepsilon + 1) \quad (2)$$

where ε was the nominal strain (mm mm^{-1}), and σ_n was the nominal stress at the corresponding strain.

The puncture resistance tests were conducted on an Instron 5944 universal testing machine by using the sample-holding apparatus and needle. The force and displacement were recorded with a needle moving speed of 50 mm min^{-1}. The device is shown in the Supplementary Fig. 10.

The authors affirm that human research participants provided informed consent for the publication of the images in Fig. 2b.

Anti-corrosion performance of coatings

The scanning frequency ranged from 10 mHz to 100 kHz with a sinusoidal voltage signal amplitude was 50 mV. The EIS experiments were performed through the CHI-660E electrochemical workstation (Shanghai Chenhua Instrument Co., Ltd) using a typical three-electrode cell. A schematic diagram of the measuring device is shown in Supplementary Fig. 11. The platinum electrode was used as the counter electrode. A saturated Ag/AgCl electrode served as the reference electrode and the steel coated by coatings served as the working electrode. The effective area of the working electrode was 1 cm^2. A Faraday shielding box aimed to avoid unnecessary outside interference, and could improve the testing accuracy for high resistance of coatings. The various impedance data were fitted with ZSimpWin software developed by Princeton Applied Research.

The large area simulated seawater immersion tests were performed to evaluate the anti-corrosion performance of coated samples. The coated samples were exposed to 5.0 wt% neutral NaCl solution at room temperature. The morphologies of the coated samples were recorded using a camera at different durations.

The scanning vibrating electrode (SVET) tests were conducted using the M370 Scanning Electrochemical Workstation (Ametek, USA). The samples were surrounded and bottom sealed with paraffin, and immersed in a 3.5 wt% NaCl solution. Before testing, the sample surface was punctured with holes in the metal surface. The tool was an embroidery needle (50 μm) with an external fixing sleeve. And the self-weight was 28.1 g. It was used to poke holes into the coating substrate and rotate it three times without applying any external force (Supplementary Fig. 12). The top of the scanning probe was deposited with a diameter of ~20 μm platinum black microspheres at a distance of 100 μm from the surface of the sample. The vibration frequencies in the x and y directions are 112 and 67 Hz, respectively, with an amplitude of 20 μm. The 25 × 25 data points were collected in each damaged area. The size of the scan area was 1 mm × 1 mm. During testing, the sample was fixed on the working platform, and the edges were sealed with paraffin. During the testing process, deionized water was added regularly to maintain a constant concentration of corrosive media. The experimental results were processed using QuikGrid software.

Two control group WPU samples were prepared, one for comparing the coating protection performance with WPU–GORM and WPU–GOLM coatings, and the other for monitoring its self-healing performance. The sample used for self-healing performance testing was soaked under punctured damage conditions for 24 h, then heated at 60 °C for 6 h for self-healing, and then monitored for current density at this time (1 h) and current density after soaking for 24 h.

Self-healing capability of WPU elastomer, WPU coating, and WPU–GOLM composite coatings

The WPU elastomer was dyed with rhodamine B, and then the splines were cut off and cross-spliced for repair (50 °C for 24 h), and tensile tests were carried out on them. At the same time, the self-healing competence of WPU elastomer was evaluated quantitatively by stress-strain curve.

The scratch self-healing ability of WPU coating on the glass was evaluated. The scalpel was used to cut a 1 mm long and 5 μm wide wound on the WPU surface. Similarly, the scratch self-healing ability of WPU–GOLM coatings on the Q235 carbon steel was also evaluated. The scalpel was used to cut a 1 mm long and 2.6 μm wide wound on the surface of WPU–GOLM. Whereupon, the samples were all placed at 50 °C for repair.

The WPU–GOLM sample was punctured with different forces using a needle tip and was exposed to a modulated fiber-guided near-infrared laser (808 nm). Then the sample was irradiated with an NIR laser. Thus, the self-healing capability of the coating after external damage, cracking, or pitting corrosion had occurred was simulated. In addition, the self-healing capability of WPU coatings was also tested by SVET.

All the experiments were performed three times to ensure reproducibility.

Characterization

Scanning electron microscopy (SEM, XL30, Philips) and MV3000 optical microscope (OM, Jiangnan Yongxin Company, China) were employed to analyze the surface morphology of bulk Gr, GO thin film, the thickness of the prepared coatings, and the self-healing performance of elastomers. An atomic force microscope (AFM, NanoScope, Digital Instruments) was employed to analyze the thickness of GO and corrosion products of the Q235 surface. Fourier transform infrared spectroscopy (FT-IR, Tensor27) was employed to check out the successful preparation of GO and WPU, and the self-healing mechanism of WPU coating. The spectra of FTIR were recorded in the range of 500–4000 cm^{-1} in a transmission mode with 1 cm^{-1} resolution.

The ^{1}H nuclear magnetic resonance (^{1}H NMR) testing was performed using Bruker's AVANCE nuclear magnetic resonance instrument. The hydrogen spectrum test frequency was 300 MHz. Zetasizer (Nano-ZS90, Malvern Instruments, UK) was employed to analyze the particle size distribution of the prepared WPU and the stability of GO in WPU polymers. The composite lotion was diluted with deionized water 100 times until it was translucent, and then it was added to the cuvette for detection.

DATA AVAILABILITY

All data generated or analyzed during this study are included in this published article (and its Supplementary Information files) and are available in the Mendeley Data repositories, https://data.mendeley.com/datasets/hsp8h8wv5c/1.

Received: 20 July 2023; Accepted: 24 November 2023;
Published online: 20 December 2023

REFERENCES

1. Liu, T. et al. Smart protective coatings with self-sensing and active corrosion protection dual functionality from pH-sensitive calcium carbonate micro-containers. *Corros. Sci.* **200**, 110254 (2022).
2. Vijayan, P. P., El-Gawady, Y. M. H. & Al-Maadeed, M. Halloysite nanotube as multifunctional component in epoxy protective coating. *Ind. Eng. Chem. Res.* **55**, 11186–11192 (2016).
3. Wang, L., Li, S. & Fu, J. Self-healing anti-corrosion coatings based on micron-nano containers with different structural morphologies. *Prog. Org. Coat.* **175**, 107381 (2023).

4. Shi, Y., Chen, C., Li, Y. & Zhao, W. Achieving dual functional corrosion resistance for epoxy coatings under alternating hydrostatic pressure via constructing P-phenylenediamine/$Ti_3C_2T_x$ hybrids. *Carbon* **201**, 1048–1060 (2023).
5. Chen, J. Y. et al. Transparent high-performance supramolecular plastics operating in all-weather environments. *Adv. Funct. Mater.* **33**, 2212564 (2023).
6. Peng, C., Chen, Z. & Tiwari, M. K. All-organic superhydrophobic coatings with mechanochemical robustness and liquid impalement resistance. *Nat. Mater.* **17**, 355–360 (2018).
7. Liu, T. et al. Extremely strengthening fatigue resistance, elastic restorability and thermodynamic stability of a soft transparent self-healing network based on a dynamic molecular confinement-induced bioinspired nanostructure. *Mater. Horiz.* **10**, 2968–2979 (2023).
8. Wu, H. et al. The biomimetic design provides efficient self-healing of ultrahigh-tough and damage-warning bio-based elastomer for protective clothing of metals. *Nano Res.* **16**, 10587–10596 (2023).
9. Hu, P. et al. A highly stretchable, fast self-healing elastomer with fast, tough, repeatable adhesion. *Chem. Eng. J.* **464**, 142543 (2023).
10. Liang, R. et al. Dual dynamic network system constructed by waterborne polyurethane for improved and recoverable performances. *Chem. Eng. J.* **442**, 136204 (2022).
11. Sun, F., Liu, L., Xu, J. & Fu, J. Smart healable polyurethanes: sustainable problem solvers based on constitutional dynamic chemistry. *Mater. Chem. Front.* **7**, 3494–3523 (2023).
12. Yao, H. et al. Water-insensitive self-healing materials: from network structure design to advanced soft electronics. *Adv. Funct. Mater.* **33**, 2307455 (2023).
13. Qiang, Y., Ran, B., Li, M., Xu, Q. & Peng, J. GO-functionalized MXene towards superior anti-corrosion coating. *J. Colloid Interface Sci.* **642**, 595–603 (2023).
14. Chen, L., Yu, Z., Yin, D. & Cao, K. Preparation and anticorrosion properties of BTA@HNTs–GO nanocomposite smart coatings. *Compos. Interfaces* **28**, 1–16 (2021).
15. Su, Y. et al. Sulfonated polyaniline assisted hierarchical assembly of graphene–LDH nanohybrid for enhanced anticorrosion performance of waterborne epoxy coatings. *Chem. Eng. J.* **426**, 131269 (2021).
16. Prasai, D., Tuberquia, J. C., Harl, R. R., Jennings, G. K. & Bolotin, K. I. Graphene: corrosion-inhibiting coating. *ACS Nano* **6**, 1102–1108 (2012).
17. Schriver, M. et al. Graphene as a long-term metal oxidation barrier: worse than nothing. *ACS Nano* **7**, 5763–5768 (2013).
18. Ding, J. H., Zhao, H. R., Zhou, M., Liu, P. L. & Yu, H. B. Super-anticorrosive inverse nacre-like graphene–epoxy composite coating. *Carbon* **181**, 204–211 (2021).
19. Zhang, Y., Tian, J., Zhong, J. & Shi, X. Thin nacre-biomimetic coating with super-anticorrosion performance. *ACS Nano* **12**, 10189–10200 (2018).
20. Ding, J., Zhao, H. & Yu, H. Bio-inspired multifunctional graphene–epoxy anticorrosion coatings by low-defect engineered graphene. *ACS Nano* **16**, 710–720 (2022).
21. Zhao, H., Ding, J., Liu, P. & Yu, H. Boron nitride-epoxy inverse "nacre-like" nanocomposite coatings with superior anticorrosion performance. *Corros. Sci.* **183**, 109333 (2021).
22. Tian, L. et al. Mutual regulation of tumour vessel normalization and immunostimulatory reprogramming. *Nature* **544**, 250–254 (2017).
23. Xu, J. et al. Room-temperature self-healing soft composite network with unprecedented crack propagation resistance enabled by supramolecular assembled lamellar structure. *Adv. Mater.* **35**, 2300937 (2023).
24. Ding, R. et al. The diffusion-dynamical and electrochemical effect mechanism of oriented magnetic graphene on zinc-rich coatings and the electrodynamics and quantum mechanics mechanism of electron conduction in graphene zinc-rich coatings. *J. Alloy. Compd.* **784**, 756–768 (2019).
25. Wong, M. et al. Large-scale self-assembled zirconium phosphate smectic layers via a simple spray-coating process. *Nat. Commun.* **5**, 3589 (2014).
26. Han, G. et al. Flexible, thermostable and flame-resistant epoxy-based thermally conductive layered films with aligned ionic liquid-wrapped boron nitride nanosheets via cyclic layer-by-layer blade-casting. *Chem. Eng. J.* **437**, 135482 (2022).
27. Yi, P. et al. Self-healable, strong, and tough polyurethane elastomer enabled by carbamate-containing chain extenders derived from ethyl carbonate. *Polymers* **14**, 1673 (2022).
28. Li, W. et al. Exploring piperazine for intrinsic weather-proof, robust and self-healable poly(urethane urea) toward surface and tire protection. *Polymer* **227**, 123829 (2021).
29. Li, Y. et al. A self-reinforcing and self-healing elastomer with high strength, unprecedented toughness and room-temperature reparability. *Mater. Horiz.* **8**, 267–275 (2021).
30. Wang, J., Wu, B., Wei, P., Sun, S. & Wu, P. Fatigue-free artificial ionic skin toughened by self-healable elastic nanomesh. *Nat. Commun.* **13**, 4411 (2022).
31. Chen, X. et al. Extremely tough, puncture-resistant, transparent, and photoluminescent polyurethane elastomers for crack self-diagnose and healing tracking. *ACS Appl. Mater. Interfaces* **12**, 30847–30855 (2020).
32. Liu, C. B. et al. Efficient graphene/cyclodextrin-based nanocontainer: synthesis and host-guest inclusion for self-healing anticorrosion application. *ACS Appl. Mater. Interfaces* **10**, 36229–36239 (2018).
33. Asaldoust, S. & Ramezanzadeh, B. Synthesis and characterization of a high-quality nanocontainer based on benzimidazole–zinc phosphate (ZP–BIM) tailored graphene oxides; a facile approach to fabricating a smart self-healing anti-corrosion system. *J. Colloid Interface Sci.* **564**, 230–244 (2020).
34. Xu, L. et al. A malleable composite dough with well-dispersed and high-content boron nitride nanosheets. *ACS Nano* **17**, 4886–4895 (2023).
35. Liu, C., Jin, Z., Zhao, H. & Wang, L. Triple-action smart nanocontainers enhanced protective coatings with superior active and passive properties. *Prog. Org. Coat.* **148**, 105887 (2020).
36. Wu, H., Cheng, L., Liu, C., Lan, X. & Zhao, H. Engineering the interface in graphene oxide/epoxy composites using bio-based epoxy-graphene oxide nanomaterial to achieve superior anticorrosion performance. *J. Colloid Interface Sci.* **587**, 755–766 (2021).
37. Hinderliter, B. R., Croll, S. G., Tallman, D. E., Su, Q. & Bierwagen, G. P. Interpretation of EIS data from accelerated exposure of coated metals based on modeling of coating physical properties. *Electrochim. Acta* **51**, 4505–4515 (2006).
38. Kartsonakis, I. A., Balaskas, A. C., Koumoulos, E. P., Charitidis, C. A. & Kordas, G. Evaluation of corrosion resistance of magnesium alloy ZK10 coated with hybrid organic-inorganic film including containers. *Corros. Sci.* **65**, 481–493 (2012).
39. Yuan, H. et al. Graphene oxide decorated with titanium nanoparticles to reinforce the anti-corrosion performance of epoxy coating. *Coatings* **10**, 129 (2020).
40. Mohammad, L. S. et al. Synthesis of graphene oxide nanosheets decorated by nanoporous zeolite-imidazole (ZIF-67) based metal-organic framework with controlled-release corrosion inhibitor performance: experimental and detailed DFT-D theoretical explorations. *J. Hazard. Mater.* **404**, 124068 (2021).
41. Li, S. et al. Bio-inspired (GO + CNTs)-PU hydrophobic coating via replication of Lotus leaf and its enhanced mechanical and anti-corrosion properties. *Prog. Org. Coat.* **159**, 106414 (2021).
42. Zhu, Q. et al. Aluminum dihydric tripolyphosphate/polypyrrole-functionalized graphene oxide waterborne epoxy composite coatings for impermeability and corrosion protection performance of metals. *Adv. Compos. Hybrid Mater.* **4**, 780–792 (2021).
43. Cheng, L., Liu, C., Zhao, H. & Wang, L. Photothermal-triggered shape memory coatings with active repairing and corrosion sensing properties. *J. Mater. Chem. A* **9**, 22509–22521 (2021).
44. Li, H., Qiang, Y., Zhao, W. & Zhang, S. 2-Mercaptobenzimidazole-inbuilt metal-organic-frameworks modified graphene oxide towards intelligent and excellent anti-corrosion coating. *Corros. Sci.* **191**, 109715 (2021).
45. Lamaka, S. V. et al. Nanoporous titania interlayer as reservoir of corrosion inhibitors for coatings with self-healing ability. *Prog. Org. Coat.* **58**, 127–135 (2007).
46. Ye, Y. et al. Superior corrosion resistance and self-healable epoxy coating pigmented with silanzied trianiline-intercalated graphene. *Carbon* **142**, 164–176 (2019).
47. Dehghani, A., Bahlakeh, G. & Ramezanzadeh, B. Designing a novel targeted-release nano-container based on the silanized graphene oxide decorated with cerium acetylacetonate loaded beta-cyclodextrin (beta-CD-CeA-MGO) for epoxy anti-corrosion coating. *Chem. Eng. J.* **400**, 125860 (2020).
48. Wang, Q. et al. Synthesis of (ZrO_2–Al_2O_3)/GO nanocomposite by sonochemical method and the mechanism analysis of its high defluoridation. *J. Hazard. Mater.* **381**, 120954 (2020).
49. Liu, T. et al. POSS-tetraaniline based giant molecule: synthesis, self-assembly, and active corrosion protection of epoxy-based organic coatings. *Corros. Sci.* **168**, 108555 (2020).
50. Kasaeian, M., Ghasemi, E., Ramezanzadeh, B., Mahdavian, M. & Bahlakeh, G. A combined experimental and electronic-structure quantum mechanics approach for studying the kinetics and adsorption characteristics of zinc nitrate hexahydrate corrosion inhibitor on the graphene oxide nanosheets. *Appl. Surf. Sci.* **462**, 963–979 (2018).
51. Kasaeian, M., Ghasemi, E., Ramezanzadeh, B., Mahdavian, M. & Bahlakeh, G. Construction of a highly effective self-repair corrosion-resistant epoxy composite through impregnation of 1H-Benzimidazole corrosion inhibitor modified graphene oxide nanosheets (GO-BIM). *Corros. Sci.* **145**, 119–134 (2018).
52. Ramezanzadeh, B., Ghasemi, E., Mahdavian, M., Changizi, E. & Mohamadzadeh Moghadam, M. H. Covalently-grafted graphene oxide nanosheets to improve barrier and corrosion protection properties of polyurethane coatings. *Carbon* **93**, 555–573 (2015).
53. Zhu, X., Zhao, H., Wang, L. & Xue, Q. Bioinspired ultrathin graphene nanosheets sandwiched between epoxy layers for high performance of anticorrosion coatings. *Chem. Eng. J.* **410**, 128301 (2021).
54. Ye, M. et al. Nanofibrillated cellulose-based superhydrophobic coating with antimicrobial performance. *Adv. Compos. Hybrid Mater.* **6**, 30 (2022).
55. Yao, B. et al. High-stability conducting polymer-based conformal electrodes for bio-/iono-electronics. *Mater. Today* **53**, 84–97 (2022).

56. GB/T 1727-2021. *General Methods for Preparation of Coating Films* [S] (Standardization Administration of the People's Republic of China. Beijing, China, 2021).

ACKNOWLEDGEMENTS

This work was supported by the National Key Research and Development Program of China (2022YFB3808800), the National Natural Science Foundation of China (52272084 and 52072177), and the Fundamental Research Funds for the Central Universities (2023102003).

AUTHOR CONTRIBUTIONS

L.W., B.W.Y., J.H.X., and J.J.F. conceived the project and designed the experiments. L.W. and X.B.W. carried out the experiments and collected and analyzed the data. T.L., F.Y.S., S.N.L., and Y.H.G. helped with the characterization of the materials and discussed data. L.W. wrote the article. B.W.Y., J.H.X., and J.J.F. revised this paper. All authors have approved the final version of the manuscript.

COMPETING INTERESTS

The authors declare no competing interests.

ADDITIONAL INFORMATION

Supplementary information The online version contains supplementary material available at https://doi.org/10.1038/s41529-023-00415-9.

Correspondence and requests for materials should be addressed to BoWen Yao, Jianhua Xu or JiaJun Fu.

Reprints and permission information is available at http://www.nature.com/reprints

Publisher's note Springer Nature remains neutral with regard to jurisdictional claims in published maps and institutional affiliations.

Open Access This article is licensed under a Creative Commons Attribution 4.0 International License, which permits use, sharing, adaptation, distribution and reproduction in any medium or format, as long as you give appropriate credit to the original author(s) and the source, provide a link to the Creative Commons license, and indicate if changes were made. The images or other third party material in this article are included in the article's Creative Commons license, unless indicated otherwise in a credit line to the material. If material is not included in the article's Creative Commons license and your intended use is not permitted by statutory regulation or exceeds the permitted use, you will need to obtain permission directly from the copyright holder. To view a copy of this license, visit http://creativecommons.org/licenses/by/4.0/.

© The Author(s) 2023